(0.2 and 0.02 wt%, respectively) onto glass in a batch reactor reveals Ni peaks at their appropriate binding energies and insignificant levels of carbon contamination (Fig. 1B). Films of similar purity are obtained when Ni depositions are performed on Pd-seeded substrates.
11. U.S. Environmental Protection Agency (EPA) "International Waste Minimization Approaches and Policies to Metal Finishing," *EPA530-R-96-008* (EPA, Washington, DC, 1996).

12. Funded by the NSF (CTS-9734177), the David and Lucile Packard Foundation, and Novellus Systems. We also acknowledge Novellus Systems for assistance with film characterization and donation of test wafers. Facilities supported by the Materials Research Science and Engineering Center at the University of Massachusetts were used for deposit characterization.

6 July 2001; accepted 29 August 2001
Published online 13 September 2001;
10.1126/science.1064148
Include this information when citing this paper.

# Organic Carbon Composition of Marine Sediments: Effect of Oxygen Exposure on Oil Generation Potential

**Yves Gélinas,[1]*† Jeffrey A. Baldock,[2] John I. Hedges[1]**

**Anaerobic sedimentary conditions have traditionally been linked to the generation of the source rocks for petroleum formation. However, the influence of sedimentary redox conditions on the composition of freshly deposited organic matter (OM) is not clear. We assessed the effect of in situ exposure time to oxic conditions on the composition of OM accumulating in different coastal and deep-sea sediments using solid-state $^{13}$C nuclear magnetic resonance (NMR). $^{13}$C NMR spectra were resolved into mixtures of model components to distinguish between alkyl carbon present in protein and nonprotein structures. There is an inverse relation between the length of exposure to oxic conditions and the relative abundance of nonprotein alkyl (alkyl$_{NP}$) carbon, whose concentration is two orders of magnitude higher in coastal sediments with short exposure times than in deep-sea sediments with long exposure times. All alkyl$_{NP}$-rich samples contain a physically separate polymethylene component similar in composition to algaenans and kerogens in type I oil shales. The duration of exposure to oxic conditions appears to directly influence the quality and oil generation potential of OM in marine shales.**

Sedimentary burial of a small fraction [<0.5% (*1–3*)] of organic matter (OM) produced in the surface ocean is responsible for the generation of fossil fuels over geologic time scales (*4–5*). Although the major precursors of these fuels are well characterized within the diagenetic continuum ranging from phytoplankton (*6–8*) to kerogens (*9–14*), the variables that control selective preservation of these "protofuels" are still debated (*15–17*). Oxygen-limited margin environments have long been associated with petroleum source rock formation (*4*) and, more recently, enhanced OM concentrations (*3*) and burial efficiencies (*16*). Yet the link between oxygen levels and the transformation of recently deposited OM into hydrogen-rich petroleum-forming kerogens is not clear. The elucidation of this link requires studies on organic carbon (OC) compositions in sediments with contrasting oxygen exposure histories. Unfortunately, such studies are hampered, because most OM in marine sediments cannot be characterized at the molecular level (*2*).

The extent of OM preservation in marine sediments appears to reflect the average period during which accumulating particles are exposed to oxic sedimentary conditions (*15*, *16*, *18*). The oxygen exposure time (OET) corresponds to the depth of $O_2$ penetration into pore waters divided by sediment accumulation rate (*3*). Such an "oxygen effect" is explained by the lower degradation rate exhibited by recalcitrant macrobiomolecules [such as pollen (*19*), lignin (*20*), cutin (*13*), hydrocarbons (*21*), and algaenans (*7*, *8*, *12*)] under anoxic as compared with oxic conditions. These molecules can be selectively preserved during anoxic diagenesis and generate fuels after thermal catagenesis (*4*, *13*). The oil generation potential of kerogens in marine shales may be determined at the first stage of diagenesis (*22*) and thus coupled to OET. If this hypothesis is valid, OM from recent diagenetically stabilized sediments with short OETs should be enriched in alkyl functional groups relative to OM from sediments with long OETs.

To test this hypothesis, we developed a demineralization method (*23*) designed to concentrate OM from marine sediments and used solid-state $^{13}$C nuclear magnetic resonance (NMR) (*24*) to compare the chemical compositions of bulk OM in 15 marine sediments representing a wide range of mineralogies and oxygen exposure histories (Table 1). These samples include an OC-rich sulfidic Black Sea sediment (sample 1) and OC-rich sediments from $O_2$-deficient zones (ODZs) along the Indian (sample 2), Peruvian (sample 3), and Mexican coasts (samples 4 and 5), as well as below (sample 6) and above (sample 7) the Mexican ODZ. Also included are sediments from the Arabian Sea (samples 8 and 9), which exhibits a productivity-driven seasonal pattern of $O_2$-deficient waters; typical margin deposits accumulating below oxygenated waters on the Washington shelf (sample 10) and upper slope (sample 11); and organic-poor sediments from the Washington coast Cascadia basin (sample 12), Southern Ocean (sample 13), and equatorial Pacific Ocean (samples 14 and 15). This sample set comprises nearshore clastic sediments and carbonate and siliceous oozes, as well as pelagic red clay sediments. $\delta^{13}$C and elemental measurements suggest that OM accumulating at these sites is predominantly marine-derived (*3*).

Major resonances corresponding to alkyl carbon [0 to 45 parts per million (ppm)] dominate all cross-polarization/magic angle spinning (CP/MAS) $^{13}$C NMR spectra (Fig. 1), with varying contributions from *N*-alkyl/methoxyl (45 to 60 ppm), *O*-alkyl (60 to 95 ppm), di-*O*-alkyl (95 to 110 ppm), aromatic/olefinic (110 to 145 ppm), phenolic (145 to 165 ppm), and carboxyl/amide (165 to 190 ppm) carbon. The seven organic-rich samples (Fig. 1, A through C) exhibit similar intensities within these chemical shift regions. Although variations in the relative contribution of each type of carbon increase among the five samples with intermediate OC concentrations (Fig. 1, D through F), resonances shapes and chemical shift values at maximum resonance intensity are similar to those obtained for organic-rich samples. Such variations between, rather than within, the different types of carbon functionalities may reflect mixtures of similar components at varying proportions. In contrast, spectra obtained for samples with low OC concentrations show greater variation in resonance shapes and relative intensities (Fig. 1, G through I). The

---

[1] School of Oceanography, Box 357940, University of Washington, Seattle, WA 98195–7940, USA. [2] Commonwealth Scientific and Industrial Research Organization (CSIRO) Land and Water, Personal Mail Box 2, Glen Osmond, South Australia 5064, Australia.

*To whom correspondence should be addressed.
†Present address: Department of Chemistry and Biochemistry, Concordia University, 1455 de Maisonneuve Boulevard West, Montreal, Quebec, Canada, H3G 1M8. E-mail: ygelinas@alcor.concordia.ca

**Table 1.** Composition of the sediment samples. $(C/N)_a$, atomic C/N ratio; ‰, per mil; D.I., diagenic degradation index.

| Sample | Depth (cm) | OC (wt%) | SA ($m^2/g$) | OC/SA ($mgOC/m^2$) | $(C/N)_a$ | $\delta^{13}C$ (‰) | Meas. OET (yrs) | Calc. OET (yrs) | D.I. | Amino acid (% of TOC) | Carbo-hydrate (% of TOC) | Black carbon (% of TOC) | $Alkyl_{NP}$ (% of TOC) | Total $Alkyl_{NP}$ (g/kg) | Total $Alkyl_{NP}/SA$ ($mg/m^2$) |
|---|---|---|---|---|---|---|---|---|---|---|---|---|---|---|---|
| 1. Black Sea | 9–11 | 4.22 | 20.2 | 2.09 | 13.03 | −24.2 | | 0.0086 | 0.3 | 27.5 | 21.5 | 15.1 | 35.8 | 15.1 | 0.75 |
| 2. Indian coast | 9–12 | 5.62 | 25.5 | 2.20 | 10.85 | −20.6 | | 0.0043 | −0.1 | 33.7 | 19.4 | 20.4 | 26.5 | 14.9 | 0.58 |
| 3. Peruvian coast | 9–11 | 7.62 | 35.0 | 2.18 | 10.29 | −20.6 | | 0.0050 | 0.2 | 31.9 | 17.3 | 20.2 | 30.6 | 23.3 | 0.67 |
| 4. Mexican coast | 9–11 | 7.59 | 36.7 | 2.07 | 10.34 | −20.9 | 0.02 | 0.0097 | −0.2 | 33.5 | 17.0 | 18.9 | 30.5 | 23.1 | 0.63 |
| 5. Mexican coast | 0–0.5 | 7.21 | 38.9 | 1.85 | 9.72 | −20.9 | 0.02 | 0.0365 | −0.3 | 34.1 | 16.4 | 22.9 | 26.6 | 19.2 | 0.49 |
| 6. Mexican coast | 9–11 | 4.23 | 35.4 | 1.19 | 10.11 | −20.8 | 0.5 | 2.03 | −0.2 | 31.9 | 15.8 | 21.7 | 30.6 | 12.9 | 0.37 |
| 7. Mexican coast | 9–11 | 3.73 | 40.2 | 0.93 | 10.40 | −20.8 | 1.0 | 10.4 | −0.3 | 33.9 | 19.4 | 17.8 | 28.8 | 10.7 | 0.27 |
| 8. Arabian Sea | 0–0.5 | 1.35 | 35.0 | 0.39 | 9.18 | −19.7 | | 278 | −0.5 | 42.8 | 21.0 | 12.8 | 23.3 | 3.2 | 0.090 |
| 9. Arabian Sea | 10–12 | 1.04 | 28.0 | 0.37 | 9.07 | −19.4 | | 304 | −0.3 | 43.6 | 18.2 | 13.8 | 24.3 | 2.5 | 0.090 |
| 10. Wash. coast | 10–12 | 2.87 | 42.0 | 0.68 | 10.16 | −22.8 | 82 | 45.4 | −0.4 | 33.0 | 18.2 | 28.4 | 20.4 | 5.9 | 0.14 |
| 11. Wash. coast | 10–12 | 1.11 | 59.3 | 0.19 | 8.24 | −23.0 | 1100 | 940 | −0.9 | 32.7 | 20.8 | 25.5 | 21.0 | 2.3 | 0.039 |
| 12. Wash. coast | 0–0.5 | 1.47 | 21.8 | 0.67 | 9.70 | −22.9 | 100 | 47.9 | −0.5 | 34.1 | 17.0 | 28.1 | 20.7 | 3.0 | 0.14 |
| 13. Southern Ocean | 9–11 | 0.33 | 20.9 | 0.16 | 8.27 | −20.8 | | 1120 | −1.5 | 40.7 | 16.1 | 30.4 | 12.9 | 0.4 | 0.020 |
| 14. Eq. Pacific 9N | 0–0.5 | 0.62 | 100.5 | 0.06 | 5.78 | −19.9 | | 2020 | −1.6 | 59.2 | 11.5 | 11.0 | 18.2 | 1.1 | 0.011 |
| 15. Eq. Pacific 9N | 10–12 | 0.31 | 90.7 | 0.03 | 4.58 | −20.4 | | 2380 | −2.0 | 75.5 | 7.5 | 4.2 | 12.9 | 0.4 | 0.0045 |

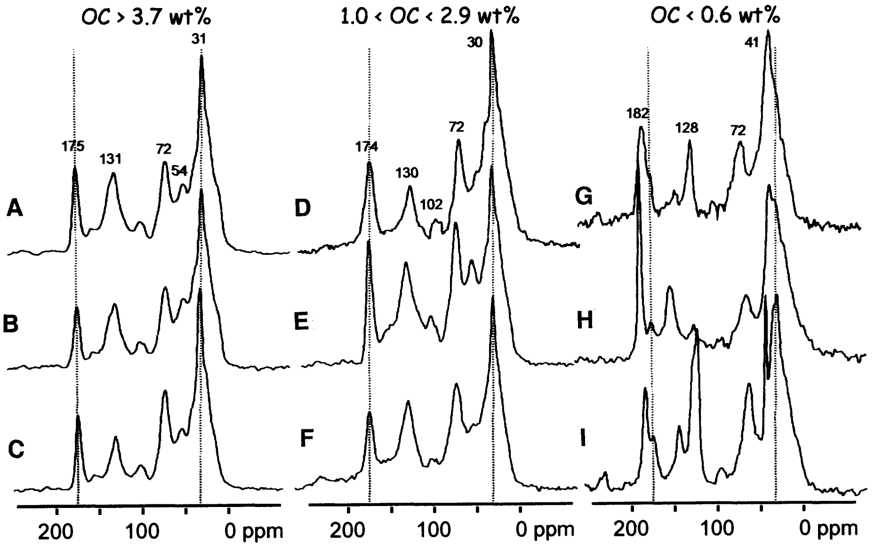

**Fig. 1.** Solid-state CP/MAS $^{13}C$ NMR spectra of demineralized sediments. Organic-rich sediments were from (**A**) the Mexican coast, (**B**) the Peruvian coast, and (**C**) the Black Sea. Sediments with intermediate OC concentrations were from (**D**) the Arabian Sea, (**E**) the Washington coast, and (**F**) the Cascadia basin west of the Washington coast. Organic-poor sediments were from (**G**) the surface and (**H**) 10 to 12 cm depth of the equatorial Pacific Ocean 9°N, and (**I**) the Southern Ocean.

maximum alkyl intensity is shifted from polymethylene (~30 ppm) to tertiary and quaternary alkyl carbon (~40 to 45 ppm). The amide/carboxylic resonance is split, probably due to the presence of carbonyl groups bonded to unsaturated or branched aliphatic carbon.

Molecular compositions were estimated by a numerical modeling procedure that used the NMR data to predict the relative fraction of OC present in biochemicals [such as amino acids, carbohydrates, nonprotein alkyl ($alkyl_{NP}$) carbon, and black carbon (*25*)] likely to be preserved in marine sediments. Such molecular mixing models allow the intensity measured for a given chemical shift region to be apportioned into fractional contributions from individual model components. Critically, $alkyl_{NP}$ carbon can then be distinguished from protein alkyl carbon to assess petroleum formation potential.

$Alkyl_{NP}$ carbon is positively correlated ($r^2 = 0.67$, $P < 0.05$) with surface area–normalized OC concentrations (Table 1). OC concentrations are normalized to surface area (*26*) to account for variations in grain size distribution and mineral composition (*27*). To assess whether this trend is linked to oxygen exposure, an estimate of OET is needed. For about half of these samples, OET values were determined in situ (*15*, *16*). For the others, we use the correlation ($r^2 = 0.96$, $P < 0.05$; Fig. 2A) between OC surface loadings and the log of OET for stations where these parameters were measured (*15*, *16*) to calculate OET from the measured OC/surface area (SA) concentrations (Table 1).

$Alkyl_{NP}$ carbon is negatively correlated ($r^2 = 0.77$, $P < 0.05$) with OET in oxic sediments (Fig. 2A). $Alkyl_{NP}$ carbon contribution is highest (26 to 36%) in anoxic sediments and decreases exponentially with increasing OET. The range of $alkyl_{NP}$ carbon contributions obtained for anoxic sediments agrees with the range of hydrogen index values [250 to 450 mg of hydrocarbon per gram of OC] measured for anoxic sediments from the Mexican (*28*), Peruvian, and Oman margins (*29*, *30*).

The relation between $alkyl_{NP}$ carbon and OET is further supported by calculating an OM degradation index based on the mole percentages of 15 hydrolyzable amino acids (*31*). The index integrates variations in the relative abundance of amino acids caused by their different rates of decomposition and alteration (*31*). For our sediment suite, the correlation ($r^2 = 0.79$, $P < 0.05$; Table 1) obtained between $alkyl_{NP}$ carbon and the degradation index provides independent evidence for an inverse relation between $alkyl_{NP}$ carbon contribution and OM degradation.

The contrasting chemical OC compositions in sediments with different OETs, coupled to the higher OC surface loadings and burial efficiencies (*16*) in sediments with short OETs, result in surface area–normalized $alkyl_{NP}$ concentrations that are more than two orders of magnitude higher in anoxic sediments than in sediments with long OETs (Fig. 2B). The correlation between normalized $alkyl_{NP}$ concentrations and OETs is significant ($r^2 = 0.92$, $P < 0.01$) for samples with measured OETs and improves to 0.96 ($P < 0.01$) when samples with calculated OETs are included. The absolute concentration of $alkyl_{NP}$ carbon, which is a pivotal determinant in the oil generation potential of source rocks, also varies by more than one

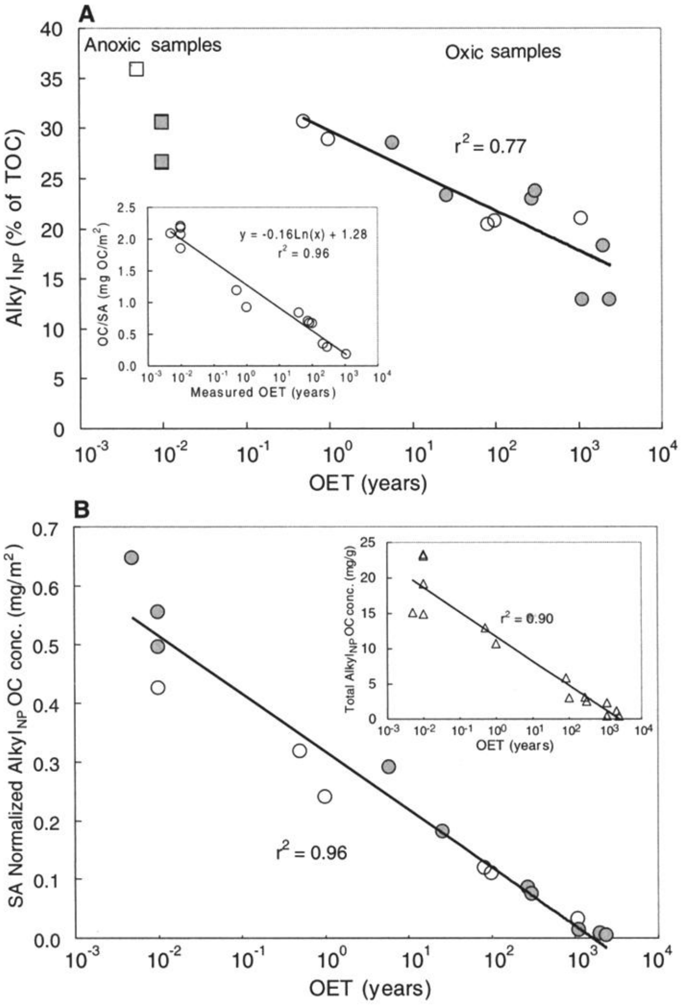

**Fig. 2.** Relative contribution of alkyl$_{NP}$ carbon (**A**) and surface area–normalized and total concentrations (insert) of alkyl$_{NP}$ carbon (**B**) plotted against measured (open circles or squares) or calculated (gray circles or squares) OET. The insert in (A) illustrates the correlation between the fraction of OC in alkyl$_{NP}$ structures and a diagenetic degradation index. The regressions are for a least-squares fit to the data for oxic sediments [circles; $y = -1.73 \ln(x) + 29.8$] in (A) and for surface area–normalized alkyl$_{NP}$ carbon concentrations [circles; $y = -0.043 \ln(x) + 0.32$] in (B).

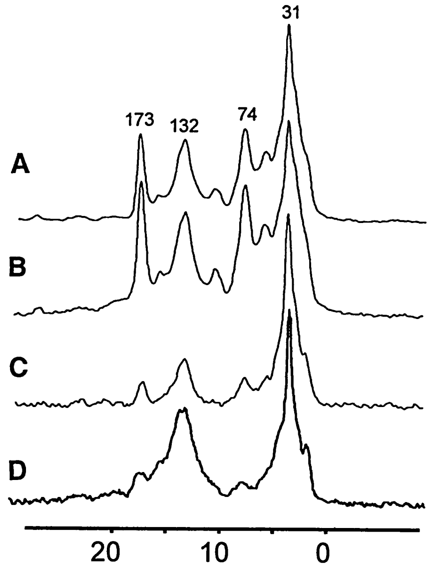

**Fig. 3.** CP/MAS spectrum of the demineralized Mexican coast sediment [(**A**), sample 5 in Table 1)] the fast-relaxing (**B**) and slow-relaxing (**C**) subspectra obtained by PSRE, and the CP/MAS spectrum of the nonhydrolyzable component of the same sample (**D**). Numbers above peaks indicate the chemical shifts (in ppm) of the major peaks.

order of magnitude over this OET range ($r^2 = 0.90$, $P < 0.05$; Fig. 2B). The better fit obtained upon normalizing concentrations to surface area suggests that selective preservation of alkyl$_{NP}$ OC may also be constrained to some extent by mineral surfaces (*27*), possibly through protective sorption (*32, 33*).

To further characterize the alkyl$_{NP}$ component, we used solid-state $^{13}$C NMR proton spin relaxation editing (PSRE) (*34*) to fractionate the acquired CP/MAS spectra and generate two subspectra of components characterized by different proton relaxation rates. These contrasting relaxation rates reflect the presence of OC components that are spatially separated by at least 30 to 100 nm (*34*). PSRE subspectra (Fig. 3) reveal that all organic-rich sediments (samples 1 through 7) are composed of two significantly different ($P < 0.05$) and physically separate components. The composition of the fast-relaxing component reflects a mixture dominated by amino acid and carbohydrate carbon. In contrast, the slow-relaxing component, which accounts for about one-third of the CP/MAS signal in OC-rich samples, is enriched in polymethylene carbon. Such PSRE distinct fractions could not be identified in samples with <3.0 weight % (wt%) OC, suggesting that OM is physically homogeneous at the nanometer scale in these samples.

We then compared the compositions of the PSRE slow-relaxing component and the nonhydrolyzable (*35*) OM fraction of the alkyl$_{NP}$-rich Mexican sediment (sample 5; Fig. 3). The nonhydrolyzable fraction accounts for 32.5% of OC and is also enriched in polymethylene carbon. Such close similarities in chemical composition and abundance (~30% of OC) between the nonhydrolyzable, alkyl$_{NP}$, and PSRE slow-relaxing components suggest that major portions of the three fractions are one and the same. This nonhydrolyzable, chemically unique, and spatially separate polymethylene component is also compositionally similar to cell wall–derived algaenans (*14*), the nonhydrolyzable component of a marine algal sapropel (*10*), and kerogen from type I oil shales (*36*).

OET thus plays an important role in the selective preservation of fossil fuel precursors in marine sediments and directly influences the oil generation potential of OM in marine shales. The early view that anaerobic conditions were essential for the generation of petroleum source rocks (*22*) appears to be an accurate first sketch of an immensely complex picture.

### References and Notes

1. U. Siegenthaler, J. L. Sarmiento, *Nature* **365**, 119 (1993).
2. S. G. Wakeham, C. Lee, J. I. Hedges, P. J. Hernes, M. L. Peterson, *Geochim. Cosmochim. Acta* **61**, 5363 (1997).
3. J. I. Hedges, R. G. Keil, *Mar. Chem.* **49**, 81 (1995).
4. B. Tissot, B. Durand, J. Espitalié, A. Combaz, *Am. Assoc. Petrol. Geol. Bull.* **58**, 499 (1974).
5. R. A. Berner, *Palaeogeogr. Palaeoclimatol. Palaeoecol.* **73**, 97 (1989).
6. P. Metzger, C. Largeau, E. Casadevall, *Prog. Chem. Org. Nat. Prod.* **57**, 1 (1991).
7. F. Gelin *et al.*, *Org. Geochem.* **26**, 659 (1997).
8. F. Gelin *et al.*, *Org. Geochem.* **30**, 147 (1999).
9. R. P. Philp, M. Calvin, *Nature* **262**, 134 (1976).
10. P. G. Hatcher, E. C. Spiker, N. M. Szeverenyi, G. E. Maciel, *Nature* **305**, 498 (1983).
11. K. Goth, J. W. de Leeuw, W. Püttmann, E. W. Tegelaar, *Nature* **336**, 759 (1988).
12. S. Derenne *et al.*, *Org. Geochem.* **19**, 345 (1992).
13. J. W. de Leeuw, C. Largeau, in *Organic Geochemistry*, M. Engel, S. A. Macko, Eds. (Plenum, New York, 1993), chap. 3.
14. H. Knicker, A. W. Scaroni, P. G. Hatcher, *Org. Geochem.* **24**, 661 (1996).
15. J. I. Hedges *et al.*, *Am. J. Sci.* **299**, 529 (1999).
16. H. E. Hartnett, R. G. Keil, J. I. Hedges, A. Devol, *Nature* **391**, 572 (1998).
17. J. I. Hedges *et al.*, *Org. Geochem.* **31**, 945 (2000).
18. G. L. Cowie, J. I. Hedges, F. G. Prahl, G. J. de Lange, *Geochim. Cosmochim. Acta* **59**, 33 (1995).
19. R. G. Keil, F. S. Hu, E. C. Tsamakis, J. I. Hedges, *Nature* **369**, 639 (1994).
20. R. Benner, A. E. MacCubbin, R. E. Hodson, *Appl. Environ. Microbiol.* **47**, 98 (1984).
21. R. M. Atlas, *Microbiol. Rev.* **45**, 180 (1981).

22. G. J. Demaison, E. T. Moore, *Am. Assoc. Petrol. Geol. Bull.* **8**, 1179 (1980).
23. Sediments were demineralized with mixtures of HCl (1N) and hydrofluoric acid (10%). Acid-soluble OM was recovered after removal of paramagnetic metals and desalting as described [Y. Gélinas, J. A. Baldock, J. I. Hedges, *Org. Geochem.* **32**, 677 (2001)].
24. Solid-state $^{13}C$ NMR is well suited for probing the bulk composition of sedimentary OM. When rigorous care is taken with spectral acquisition techniques [P. Kinchesh, D. S. Powlson, E. W. Randall, *Eur. J. Soil Sci.* **46**, 125 (1995)], $^{13}C$ NMR can provide a representative estimate of all OC forms in a sample.
25. P. N. Nelson, J. A. Baldock, P. Clarke, J. M. Oades, G. J. Churchman, *Aust. J. Soil Res.* **37**, 289 (1999). Biochemical compositions and an application of the model can be found in Hedges et al. [*Nature* **409**, 801 (2001)]. For this work, however, oleic acid was used as the lipid component rather than stearic acid, and the calculated fraction of OC present in protein structures was not constrained by the N:C ratio of the sample.
26. Surface areas were obtained by Brunaer-Emmett-Teller adsorption isotherms using $N_2$ as the adsorbent.
27. M. J. Bock, L. M. Mayer, *Mar. Geol.* **163**, 65 (2000).
28. R. S. Ganeshram, S. E. Calvert, T. F. Pedersen, G. L. Cowie, *Geochim. Cosmochim. Acta* **63**, 1723 (1999).
29. A. Lückge, M. Boussafir, E. Lallier-Vergès, R. Littke, *Org. Geochem.* **24**, 437 (1996).
30. S. M. Henrichs, in *Organic Geochemistry*, M. H. Engel, S. A. Macko, Eds. (Plenum, New York, 1993), pp. 101–117.
31. B. Dauwe, J. J. Middelburg, P. M. J. Herman, C. H. R. Heip, *Limnol. Oceanogr.* **44**, 1809 (1999). Spiked samples were hydrolyzed (with 6N HCl at 150°C for 70 min in $N_2$). Amino acids were then reacted with o-phthaldialdehyde and analyzed by reverse-phase high-performance liquid chromatography.
32. V. Salmon, S. Derenne, E. Lallier-Vergès, C. Largeau, B. Beaudouin, *Org. Geochem.* **31**, 463 (2000).
33. R. G. Keil, D. B. Montluçon, F. G. Prahl, J. I. Hedges, *Nature* **370**, 549 (1994).
34. R. J. Smernik, J. O Skjemstad, J. M. Oades, *Aust. J. Soil. Res.*, **38**, 665 (2000).
35. The nonhydrolyzable component was obtained after demineralization and sequential hydrolyses to remove carbohydrates (with 2N to 6N trifluoroacetic acid at 100°C in $N_2$) and proteins (with 6N HCl at 150°C in $N_2$).
36. M. A. Wilson, *NMR Techniques and Applications in Geochemistry and Soil Chemistry* (Pergamon, Oxford, 1987).

37. We thank R. Keil, S. Wakeham, the University of Washington Marine Organic Geochemistry and CSIRO groups, and two anonymous reviewers for their inputs into this manuscript. Supported by NSF grants to J.I.H. and a Canadian NSERC fellowship to Y.G.

8 May 2001; accepted 24 August 2001

---

# Late Holocene Climate and Cultural Changes in the Southwestern United States

**Victor J. Polyak* and Yemane Asmerom**

**Columnar stalagmites in caves of the Guadalupe Mountains during the late Holocene record a 4000-year annually resolved climate history for the southwestern United States. Annual banding, hiatuses, and high-precision uranium-series dating show a present day–like climate from 4000 to 3000 years ago, following a drier middle Holocene. A distinctly wetter and cooler period from 3000 to 800 years ago was followed by a period of present day–like conditions, with the exception of a slightly wetter interval from 440 to 290 years before the present. The stalagmite record correlates well with the archaeological record of changes in cultural activities of indigenous people. Such climate change may help to explain evidence of dwelling abandonment and population redistribution.**

We present high-resolution late Holocene climate reconstruction for the southwestern United States on the basis of variations in annual band thickness, growth–no growth records, differences in mineralogy, and high-precision uranium-series (U-series) dating of stalagmites. These stalagmites, from Carlsbad Cavern and Hidden Cave, Guadalupe Mountains, New Mexico (Fig. 1), show evidence of primary features such as aragonite layers, well-preserved delicate fossils, and growth banding, indicating a lack of diagenetic alteration. Aragonite layers in calcitic stalagmites generally form at the typically low cave temperature (i.e., 20°C) under conditions of higher-than-normal evaporation from already elevated Mg/Ca in cave waters, and can therefore be regarded (in comparison to calcite layers) as indicators of more evaporative conditions in caves (*1–4*). Changes in species of well-preserved fossil mites and other microarthropod parts may also be broad indicators of climate change (*5*). Annual growth banding in stalagmites, documented elsewhere by only a few reports (*3, 6–9*), has the potential to reveal highly resolved climate change. In this semi-arid region with seasonal-dependent precipitation, stalagmite growth is moisture limited, and with relative humidity of 75 to 95% in these caves, the stalagmites—although not yet useful for stable isotope work (*10*), unlike other settings (*2, 11*)—preserve well-defined, climate-revealing, annual bands.

Layers of altering clear and inclusion-rich calcite [couplets (*8, 9*)] define annual banding in the stalagmites, which can be detected by optical microscopy (Fig. 2). Our darker inclusion-rich portions of each couplet appear to consist of a mixture of water and organics probably formed by a dry-seasonal deposition of microflora. The clear portion of each band represents faster growth during seasonal periods of increased drip rates. To establish that the bands constitute annual deposition of calcite, we measured thicknesses of >1600 bands (from a possible ~2000 bands, 2796 ± 88 to 835 ± 25 years B.P.) in stalagmite BC2. The average measured band thickness equals 0.106 ± 0.002 mm/year, and the growth rate derived from U-series dating equals 0.100 ± 0.006 mm/year, which are within their $2\sigma$ errors (*12, 13*). There are no apparent hiatuses in this segment of stalagmite BC2, and it is clear that the bands represent annual deposition of calcite, and that band thickness represents the growth rate. This agreement was strengthened by supporting data from all five stalagmites (*13*). It is also apparent that decreased annual precipitation usually results in thinner bands, aragonite layers, or no-growth scenarios. For instance, a sequence of thinner bands in stalagmite BC2 was deposited coeval with aragonite layers in stalagmites 89029 and 89037. In our climatic setting, thicker calcite bands are therefore interpreted as relative indicators of increased annual precipitation like that reported by Brook *et al.* (*9*).

A significantly cooler, wetter climate in the

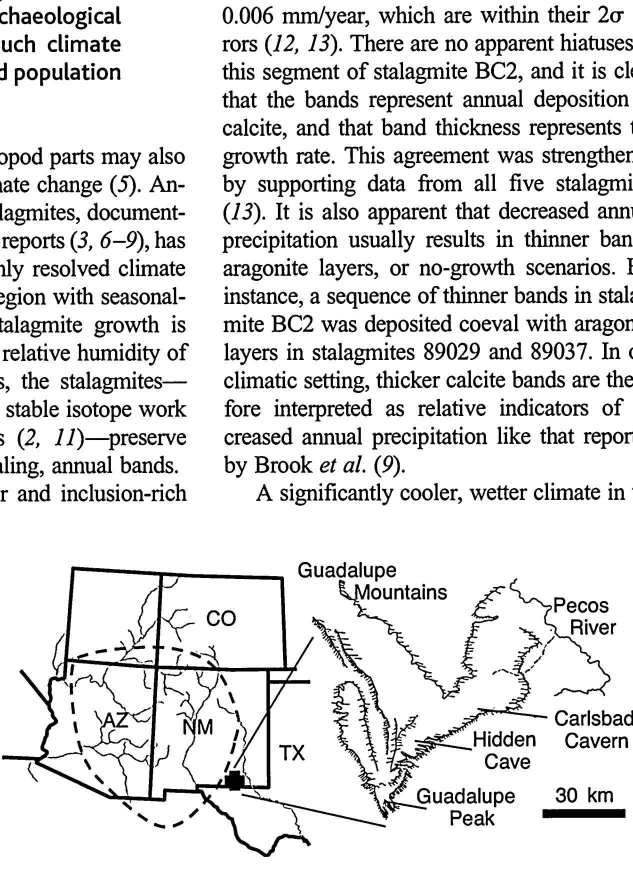

**Fig. 1.** Location of Carlsbad Cavern, Hidden Cave, and the Guadalupe Mountains in relation to the puebloan Southwest (dashed line). Samples from Carlsbad Cavern came from the entrance to Bat Cave near the commercial trail. Collection location of Hidden Cave samples is given in (*5*).

---

Department of Earth and Planetary Sciences, University of New Mexico, 200 Yale Boulevard, Albuquerque, NM 87131, USA.

*To whom correspondence should be addressed. E-mail: polyak@unm.edu